



High entropy brasses and bronzes – Microstructure, phase evolution and properties

Kevin J. Laws ^a, Cody Crosby ^b, Aarthi Sridhar ^b, Patrick Conway ^a, Leah S. Koloadin ^c, Mo Zhao ^b, Shifrah Aron-Dine ^b, Lori C. Bassman ^{b,*}

^a School of Materials Science and Engineering, University of New South Wales, NSW 2052, Australia

^b Department of Engineering, Harvey Mudd College, 301 Platt Blvd, Claremont, CA 91711, USA

^c Mark Wainwright Analytical Centre, Electron Microscope Unit, University of New South Wales, NSW 2052, Australia



ARTICLE INFO

Article history:

Received 30 June 2015

Received in revised form

29 July 2015

Accepted 30 July 2015

Available online 1 August 2015

Keywords:

High entropy alloys

Metals and alloys

Disordered systems

Solid solution

Crystal structure

Magnetically ordered materials

ABSTRACT

A family of new high entropy, or compositionally complex, alloy brasses and bronzes has been developed with strengths and hardnesses considerably higher than those of conventional brasses and bronzes and exceptional compressive ductility. By utilising the extended solid solution range of the ternary Cu–Mn–Ni alloy system, stepwise additions of Al, Sn and/or Zn have been added to an equiatomic CuMnNi alloy base. The resulting fcc and bcc crystal structures often follow similar phase evolution trends to those observed in regular brasses and bronzes as Al, Sn and Zn solute contents increase. Due to specific structural ordering, some of these alloys exhibit respectable soft magnetic properties. Reported are the specific microstructures, phase evolution upon heat treatment, mechanical properties and observed basic magnetic response of these alloys.

© 2015 Elsevier B.V. All rights reserved.

1. Introduction

Brasses and bronzes are amongst the earliest of alloyed metals, first appearing around 5000 BC and thought to be produced from a single Zn-rich ore [1,2]. In the Roman era from 1000 BC were the first known instances of true, controlled alloying to form brasses, done by reacting individual metals or metal ores in specific quantities (probably to maximise the “gold” colour of the alloy) [3,4]. The broad range of applications of modern brasses and bronzes is subtly astounding: from the keys in your pocket (often chrome plated), the key-ring they are on, the hinges of your home's front door, the door knobs and all their internal locking mechanisms, your bathroom fixtures, domestic plumbing, and the zippers on your clothes and bags, all the way to electronic hardware, gears in gear motors, bezels and badges, military munitions cartridges and highly corrosion resistant marine fixtures. Brasses are also the largest constituent of world coin currencies. Without doubt, brasses and bronzes are the most widely utilised family of metals. Modern brasses exhibit exceptional combinations of strength, formability,

durability, machinability and corrosion resistance [5,6].

Typical modern brasses and bronzes consist of a copper base with substantial alloying additions of zinc (brasses), tin, silicon or aluminium (bronzes) and often small amounts of phosphorus or lead for improved properties or machinability [5,6]. Other brass-like alloys such as nickel silvers (Cu–Ni–Zn) and manganese bronze (Cu–Mn–Zn) behave quite similarly to Cu–Zn brasses [5,6].

Copper-rich or alpha-(α -) brasses and bronzes tend to maintain their disordered face-centred-cubic (fcc) crystal structure (A1) up to their relatively large solute solubility limits, beyond which an ordered body-centred-cubic (bcc) phase (B2) denoted as beta (β) is stable. The α phase has a lower strength and is considerably more ductile than the stronger, harder β phase. The higher the amount of dissolved alloying elements Al, Sn or Zn within either phase, the greater the contribution to solute strengthening. Typically, forming brasses are completely or predominantly α , whereas stronger, harder brasses for wear resistant or mechanical applications are duplex α + β microstructures [5,6].

Recently a new type of advanced, multicomponent alloy has been proposed, often labelled “high entropy” or more aptly “compositionally complex” alloys (HEAs or CCAs). Generally these alloys consist of at least four elemental components with substantial content of each. In most cases they are found or engineered

* Corresponding author.

E-mail address: bassman@hmc.edu (L.C. Bassman).

to primarily contain one or two simple solid solution phases with high thermal and long-term microstructural stability. The yield strengths and ductilities of HEAs can be quite impressive due to unique extended solid-solution strengthening and dislocation/stacking fault mechanisms. Further, HEAs are known to exhibit decent corrosion and fatigue resistance [7–18].

To date, the majority of HEAs have been based on the mutually soluble mid-transition metals Fe–Co–Ni, often in combination with Cr, Mn and/or V [7–10] and further additions of Al, Ti and/or Nb [10–14]. In addition, refractory metal-based systems have been created using mutually soluble combinations of Zr–Ti–Hf, Nb–Ta–V and W–Mo–Cr systems [12,15–19]. Most recently rare-earth metal-based hexagonal Y–Gd–Tb–Dy–Lu, Gd–Tb–Dy–Tm–Lu and Ho–Dy–Y–Gd–Tb single phase alloys have also been reported [20,21].

In this research, the mutually soluble Cu–Mn–Ni ternary system is explored to generate a new family of HEAs. Stepwise additions/combinations of Al, Sn and Zn, which are soluble in Cu, Mn and Ni, are added to the equiatomic CuMnNi ternary composition to form novel quaternary and quinary high entropy brass- or bronze-like alloys consisting of one or two phases. The microstructures, phase evolution upon heat treatment, mechanical properties and basic magnetic properties of these new alloys are reported.

2. Alloy design concept

Strukturbericht notation is used herein to represent the different phase types present in these alloys. A1 refers to a disordered fcc phase, similar to that of pure Cu or α -brass. B1 refers to an ordered fcc phase closely related to the L1₂ structures of Ni₃Al and Ni₃Mn intermetallic compounds. The H-L1₂ designation represents a typical Heusler-type L1₂ crystal structure with a degree of magnetic ordering. B2 refers to an ordered bcc crystal structure similar to that found in CuZn (β -Brass), NiAl and MnNi. A range of crystal structure representatives and range of related binary and ternary phase diagrams is available in the [Supplementary information section \(online version\)](#).

The alloy design concept behind this work is centred about the ternary Cu–Mn–Ni system. The disordered fcc (A1 prototype) solid solution between Cu and Ni can sustain 10–20 at% of dissolved Mn [22,23]. Low-temperature ordering has been found to exist in the Cu–Mn binary system [24] and an ordered L1₂ phase is also present in this ternary system based on the binary Ni₃Mn intermetallic compound, again with reasonable Cu solubility [25]. For creation of a high entropy alloy system, the region of interest would lie at an equiatomic CuMnNi alloy composition where it is reported that two fcc phases co-exist, namely the disordered (A1) fcc solid solution and an ordered (L1₀) fcc phase based on the MnNi intermetallic (that exhibits substantial solubility of Cu). Despite this, after heat treatment at 850 °C for 18 h, the equiatomic CuMnNi alloy exhibited a single phase fcc solid solution microstructure, with no resolvable compositional fluctuation throughout the sample or indication of specific L1₀ or L1₂ phases.

Ni and Mn are two of the typical additions to Cu in modern alloy brasses and bronzes. Based on evidence from equilibrium binary and ternary phase diagrams of these three base elements with other common additions, Al, Sn and Zn have been selected as further additions to form quaternary alloys. With understanding gained from the quaternary alloys, promising quinary alloys were developed.

2.1. Cu–Mn–Ni–Al quaternary alloys

The maximum solubility of Al in fcc Cu is below 18 at% [26]. The solubility of Al in the low temperature polymorph of Mn (A12) is

also around 18 at%, however as much as 32 at% Al is soluble in the higher temperature β -Mn structure (A13). On the other hand, the solubility limit of Al in Ni is below 10 at% [27]. The Cu₂MnAl and Ni₂MnAl intermetallic compositions exhibit a specifically ordered L1₂ crystal structure, commonly known as a Heusler structure, with unique magnetic properties [28].

2.2. Cu–Mn–Ni–Sn quaternary alloys

The solubility of Sn in fcc Cu is approximately 1 at%. A high temperature A2 phase denoted as Cu_{0.85}Sn_{0.15} does exist, however the first equilibrium phase stable at room temperature is an A3-type Cu₃Sn phase [29]. Sn has limited solubility in the low temperature Mn lattice of around 2 at%, however it maintains a relatively high solubility between 6 and 10 at% in the high temperature β -Mn (A13) structure [30]. Sn also has limited solubility (<1 at% at room temperature) in fcc Ni, but a high temperature Ni₃Sn phase with a cubic DO₃ structure exists [31]. The reported Cu₂MnSn and Ni₂MnSn ternary intermetallic compounds (Heusler-type alloys) have an L1₂ type crystal structure and display specific (magnetic) ordering [32,33].

2.3. Cu–Mn–Ni–Zn quaternary alloys

The maximum low temperature solubility of Zn in Cu is approximately 30 at%. Cu-rich alloys within this phase field are known as α -brasses and have a fcc (A1) crystal structure [34]. Beyond this Zn concentration, the ordered bcc (B2) β -phase becomes stable, producing either a duplex α + β microstructure or completely β at Zn concentrations beyond approximately 43 at%. The β phase is considerably harder, stronger and more brittle than α , hence higher Zn-containing alloys reflect these properties. In the Mn–Zn system [35], Zn has limited solubility in the low temperature structure of Mn, however it maintains a solubility between 20 and 32 at% in the high temperature β -Mn (A13) structure. The low temperature MnZn phase present at higher Zn content also has an ordered bcc (B2) phase, similar to that of the CuZn (β -brass) phase. The solubility of Zn in fcc Ni is approximately 27 at% [36]. The phase equilibria are similar to those of Cu–Zn and Mn–Zn, however in this case the high temperature NiZn phase has an ordered bcc (B2) structure and the low temperature NiZn phase has a tetragonal (B11) structure [36], which is essentially an ordered arrangement of the bcc structure [37].

3. Experimental procedures

3.1. Alloying, casting and heat treatment

The nominal compositions of alloys produced in this work are shown in [Tables 1–4](#). Pure elements Cu (99.95 wt.%), Mn (99.8 wt.%) and Ni (99.95 wt.%) were alloyed using a Buhler MAM1 arc melter in a Ti-gettered argon (99.999 vol.%) atmosphere to produce a ternary master alloy. Ternary alloy ingots were turned and melted five times to ensure homogeneity. Care was also taken to ensure a sufficiently low melt superheat to avoid the evaporation of Mn. Quaternary and quinary alloy ingots containing Zn were alloyed using an induction furnace by combining the equiatomic CuMnNi master alloy with pure Zn (99.99 wt.%) in a boron nitride-coated graphite crucible. These alloys were heated in a step-wise fashion with sufficient holding times at 700 °C, 900 °C and 1050 °C to enable the dissolving of the master alloy in Zn in order to minimise Zn evaporation, yet produce a homogeneous alloy. Once a steady Zn evaporation rate was determined for this alloying process, excess Zn was added to these alloys to compensate for this loss. Quaternary alloys containing Al or Sn were produced by adding the

Table 1Alloys prepared in the quaternary $[CuMnNi]_{100-x}Al_x$ alloy system, their as-cast and heat treated microstructures, hardnesses and compressive yield strengths and ductilities.

Composition	Crystal structures and phase volume fractions (in parentheses)		Hardness (Vickers)		Yield strength (MPa)	Ductility (comp. Strain)
	As-cast	Heat treated	As-cast	Heat treated		
$[CuMnNi]_{95}Al_5$	A1 ⁽¹⁰⁰⁾	A1 ⁽⁸⁰⁾ + B1 ⁽²⁰⁾	166 ± 12	174 ± 3	330 ⁺¹⁰ ₋₄₀	>45%
$[CuMnNi]_{90}Al_{10}$	A1 ⁽⁴⁸⁾ + B1 ⁽⁵²⁾	A1 ⁽⁴³⁾ + B1 ⁽⁵⁷⁾	241 ± 3	220 ± 4	515 ⁺¹⁵ ₋₅₅	40%
$[CuMnNi]_{80}Al_{20}$	A1 ⁽⁴⁶⁾ + H-L2 ⁽⁵⁴⁾	B1 ⁽²⁰⁾ + H-L2 ⁽⁸⁰⁾	346 ± 8	355 ± 9	—	—
$[CuMnNi]_{75}Al_{25}$	B1 ⁽⁵³⁾ + H-L2 ⁽⁴⁷⁾	H-L2 ⁽¹⁰⁰⁾	377 ± 2	373 ± 5	—	—
$[CuMnNi]_{70}Al_{30}$	H-L2 ⁽⁵³⁾ + B2 ⁽⁴⁷⁾	H-L2 ₁ + B2 ^b	355 ± 10	359 ± 10	—	—
$[CuMnNi]_{60}Al_{40}$ ^a	H-L2 ⁽⁵⁷⁾ + B2 ⁽⁴³⁾	H-L2 ₁ + B2 ^b	395 ± 3	398 ± 17	—	—

^a Sample showed some segregation of Al in as-cast state and evidence of spinodal decomposition in the heat treated state.^b Phase volume fractions not distinguishable.**Table 2**Alloys prepared in the quaternary $[CuMnNi]_{100-x}Sn_x$ alloy system, their as-cast and heat treated microstructures, hardnesses and compressive yield strengths and ductilities.

Composition	Crystal structure and phase volume fractions (in parentheses)		Hardness (Vickers)		Yield strength (MPa)	Ductility (comp. Strain)
	As-cast	Heat treated	As-cast	Heat treated		
$[CuMnNi]_{95}Sn_5$	A1 ⁽⁸¹⁾ + H-L2 ₁ ⁽¹⁹⁾	A1 ⁽⁸³⁾ + H-L2 ₁ ⁽¹⁷⁾	205 ± 8	178 ± 6	380 ⁺¹⁰ ₋₃₀	>63%
$[CuMnNi]_{90}Sn_{10}$	A1 ⁽²⁶⁾ + H-L2 ₁ ⁽⁷⁴⁾	A1 ⁽⁵⁰⁾ + H-L2 ₁ ⁽⁵⁰⁾	318 ± 4	255 ± 16	620 ⁺¹²⁵ ₋₁₀₅	20%
$[CuMnNi]_{80}Sn_{20}$	A1 ⁽⁵⁾ + H-L2 ₁ ⁽⁹⁵⁾	A1 ⁽⁸⁾ + H-L2 ₁ ⁽⁹²⁾	402 ± 2	533 ± 15	—	—
$[CuMnNi]_{75}Sn_{25}$	H-L2 ₁ ⁽¹⁰⁰⁾	~H-L2 ₁ ⁽⁹⁹⁾	467 ± 20	507 ± 37	—	—

Table 3Alloys prepared in the quaternary $[CuMnNi]_{100-x}Zn_x$ alloy system, their as-cast and heat treated microstructures, hardnesses and compressive yield strengths and ductilities.

Composition	Crystal structure and phase volume fractions (in parentheses)		Hardness (Vickers)		Yield strength (MPa)	Ductility (comp. Strain)
	As-cast	Heat treated	As-cast	Heat treated		
$[CuMnNi]_{80}Zn_{20}$	A1 ⁽¹⁰⁰⁾	A1 ⁽¹⁰⁰⁾	109 ± 7	113 ± 3	140 ⁺⁵ ₋₅	>65%
$[CuMnNi]_{75}Zn_{25}$	A1 ⁽¹⁰⁰⁾	A1 ⁽¹⁰⁰⁾	147 ± 6	128 ± 10	215 ⁺⁵ ₋₂₀	>60%
$[CuMnNi]_{65}Zn_{35}$	A1 + B2 ^a	A1 ^(>95) + B2 ^(<5) ^b	246 ± 7	242 ± 9	—	—
$[CuMnNi]_{60}Zn_{40}$	A1 + B2 ^a	A1 ⁽⁸⁵⁾ + B2 ⁽¹⁵⁾ ^b	268 ± 5	253 ± 4	—	—

^a Phase volume fractions not determined.^b Limited accuracy due to low volume fraction.**Table 4**Alloys prepared in the quinary $[CuMnNi]_{100-x-y-z}Al_xSn_yZn_z$ alloy systems, their as-cast and heat treated microstructures and hardnesses.

Composition	Crystal structure and phase volume fractions (in parentheses)		Hardness (Vickers)		Heat treated
	As-cast	Heat treated	As-cast	Heat treated	
$[CuMnNi]_{90}Al_5Sn_5$	[A1+B1] ⁽⁴⁵⁾ + H-L2 ₁ ⁽⁵⁵⁾	A1 ⁽⁴⁰⁾ + H-L2 ₁ ⁽⁶⁰⁾	297 ± 4	303 ± 9	
$[CuMnNi]_{75}Al_5Zn_{20}$	A1 ⁽⁷⁸⁾ + H-L2 ₁ ⁽²²⁾	A1 + H-L2 ₁ ^a	233 ± 9	271 ± 9	
$[CuMnNi]_{60}Al_5Zn_{35}$	A1 ⁽⁶⁾ + B1 ⁽¹³⁾ + B2 ⁽⁸¹⁾	B1 ⁽¹⁴⁾ + B2 ⁽⁸⁶⁾	295 ± 8	281 ± 10	
$[CuMnNi]_{80}Al_{10}Zn_{10}$	A1 ⁽⁷⁰⁾ + H-L2 ₁ ⁽³⁰⁾	A1 ⁽²⁵⁾ + H-L2 ₁ ⁽⁷⁵⁾	257 ± 11	321 ± 2	
$[CuMnNi]_{70}Al_{10}Zn_{20}$	A1 ⁽⁸¹⁾ + H-L2 ₁ ⁽¹⁹⁾	A1 ⁽⁵¹⁾ + H-L2 ₁ ⁽⁴⁹⁾	228 ± 12	306 ± 9	
$[CuMnNi]_{75}Sn_5Zn_{20}$	A1 ⁽²⁴⁾ + H-L2 ₁ ⁽⁷⁶⁾	A1 ⁽⁴⁵⁾ + H-L2 ₁ ⁽⁵⁵⁾	278 ± 8	286 ± 10	
$[CuMnNi]_{60}Sn_5Zn_{35}$	A1 ⁽⁷⁵⁾ + H-L2 ₁ ⁽²⁵⁾	A1 + H-L2 ₁ + Mn ^{+a}	362 ± 4	376 ± 5	
$[CuMnNi]_{70}Sn_{10}Zn_{20}$	>3 phases	A1 ⁽³⁵⁾ + H-L2 ₁ ⁽⁵⁶⁾ + Mn ^{+b}	345 ± 9	372 ± 15	

^a Phase volume fractions not determined.

balance of Al (99.99 wt.%) or Sn (99.95 wt.%) to the equiatomic CuMnNi, arc melting and vacuum casting into a copper mould to produce 3 mm diameter rods. Samples were heat treated in an elevator furnace at 850 °C for 18 h under a circulating argon atmosphere and then quenched in water.

3.2. Composition and crystal structure determination

Samples were examined by optical microscopy (Leica DM6000) and scanning electron microscopy (SEM) using a Carl Zeiss AURIGA CrossBeam Workstation with a field emission scanning electron microscope and energy dispersive X-ray spectroscopy (EDS) and

electron backscattered diffraction (EBSD) capabilities. Using pure metal standards, EDS was performed using an Oxford Instruments X-Max detector. In both single and multi-phase samples, compositions were analysed over large areas and found to be within ±1.7 at% of nominal compositions (including excess Zn additions to compensate for evaporation). With the overall composition confirmed as an effective additional standard within expected error, compositions of individual phases in multi-phase alloys could be measured with sufficient confidence. Samples that did not show composition contrast using the backscattered electron detector were etched in 2 vol.% HNO₃ solution until the microstructure was suitably revealed.

A combination of EBSD and powder X-ray diffraction (XRD) techniques were used to identify the crystal structures of individual phases within alloy compositions. Kikuchi patterns (EBSD) were acquired using a NordlysF electron backscatter detector with an accelerating voltage of 10 kV. Identification of crystal structure was performed using Oxford Instruments EBSD software AZtecHKL (see Fig. 1). XRD was performed using the PANalytical Xpert Multipurpose X-ray Diffraction System using a Cu K α radiation source. Powdered samples were used to avoid intensity bias in diffraction peaks due to texture. Brittle samples were prepared by crushing in a high impact mortar and pestle and then powdering using a ring mill. Ductile sample powders were prepared using a carbon steel file. Volume fractions of phases were determined ($\pm 5\%$ max) from phase contrast in backscatter SEM images using custom code developed from the image processing toolbox in Matlab (Mathworks, Inc.). XRD results were used to both confirm or determine (when phases could not be resolved visually from micrographs) phase volume fractions and lattice parameters.

3.3. Mechanical testing

Vickers microhardness measurements were conducted on the samples using a Struers DuraScan (Struers A/S) with a 1 kg load held for 10 s. Samples were polished to a 3 micron finish before testing and at least five measurements (spaced five indent widths away from each other) were made on each sample. Cylindrical compression samples with a 3 mm diameter and 2:1 length-to-diameter ratio were ground from bulk samples using an Optical Magnified Facet jeweler's lap (Poly-Metric Instruments, Inc.) to a 600-grit final surface finish. Compression tests were performed on the cylindrical samples using an Instron 5982 test bed. Samples were tested under uniaxial compression with a constant crosshead speed corresponding to an initial strain rate of 0.005 (mm/mm)/min.

3.4. Magnetism

A common 1.1 T Fe–Nd–B permanent magnet was used to test whether magnetic attraction was present in the as-cast and heat treated samples and whether magnetisation was permanent/residual (hard magnetic materials) or non-permanent (soft magnetic).

4. Results and analysis

4.1. Ternary Cu–Mn–Ni system

The compressive stress–strain curve for the CuMnNi heat treated alloy with a grain size of $>300\text{ }\mu\text{m}$ (test was stopped at 40% compressive strain) is shown for comparison in each of the quaternary compression test figures in Sections 4.2–4.4. The yield strength was found to be between 200 and 220 MPa which is comparable to that of annealed Cu (~200 MPa) or Ni (~170 MPa) and unlike pure Mn, the sample was found to be exceptionally ductile and confirmed as a sound alloy base for this work.

4.2. Cu–Mn–Ni–Al quaternary alloys

Table 1 lists the range of alloys prepared in the [CuMnNi]_{100-x}Al_x quaternary alloy system, along with the phase types present in their microstructures and hardness in the as-cast and heat treated conditions. Figs. 2 and 3 show the as-cast and heat treated microstructures of the [CuMnNi]_{100-x}Al_x alloys, which have microstructures with one or two phases and simple microstructural evolution of the as-cast and heat treated microstructures as the Al content is increased.

The microstructure of the as-cast [CuMnNi]₉₅Al₅ alloy shown in Fig. 2(a) exhibits a homogeneous (disordered) fcc crystal structure upon casting into a water cooled copper mould as a 3 mm rod

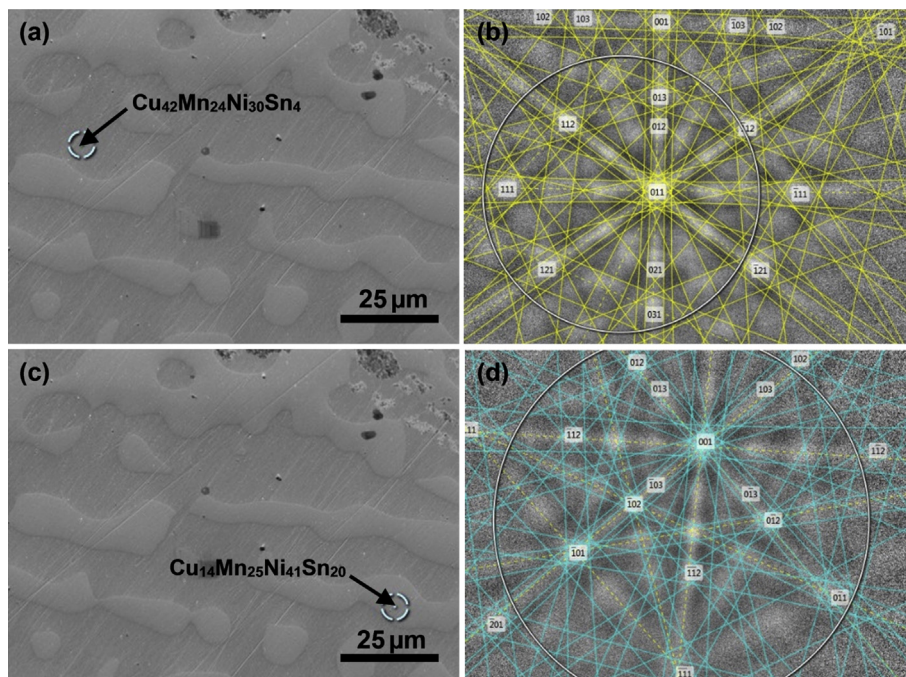


Fig. 1. Composition determination and EBSD indexing of the two-phase heat treated [CuMnNi]₉₀Sn₁₀ alloy (indexed and composition regions indicated by light blue circles) showing (a) the dark phase of composition $\text{Cu}_{42}\text{Mn}_{24}\text{Ni}_{30}\text{Sn}_{4}$ indexing as a fcc crystal structure in (b), and (c) the light phase of composition $\text{Cu}_{14}\text{Mn}_{25}\text{Ni}_{41}\text{Sn}_{20}$ indexing as a bcc crystal structure (the sub-lattice structure of the Heusler-L₁ crystal) in (d). (For interpretation of the references to colour in this figure legend, the reader is referred to the web version of this article.)

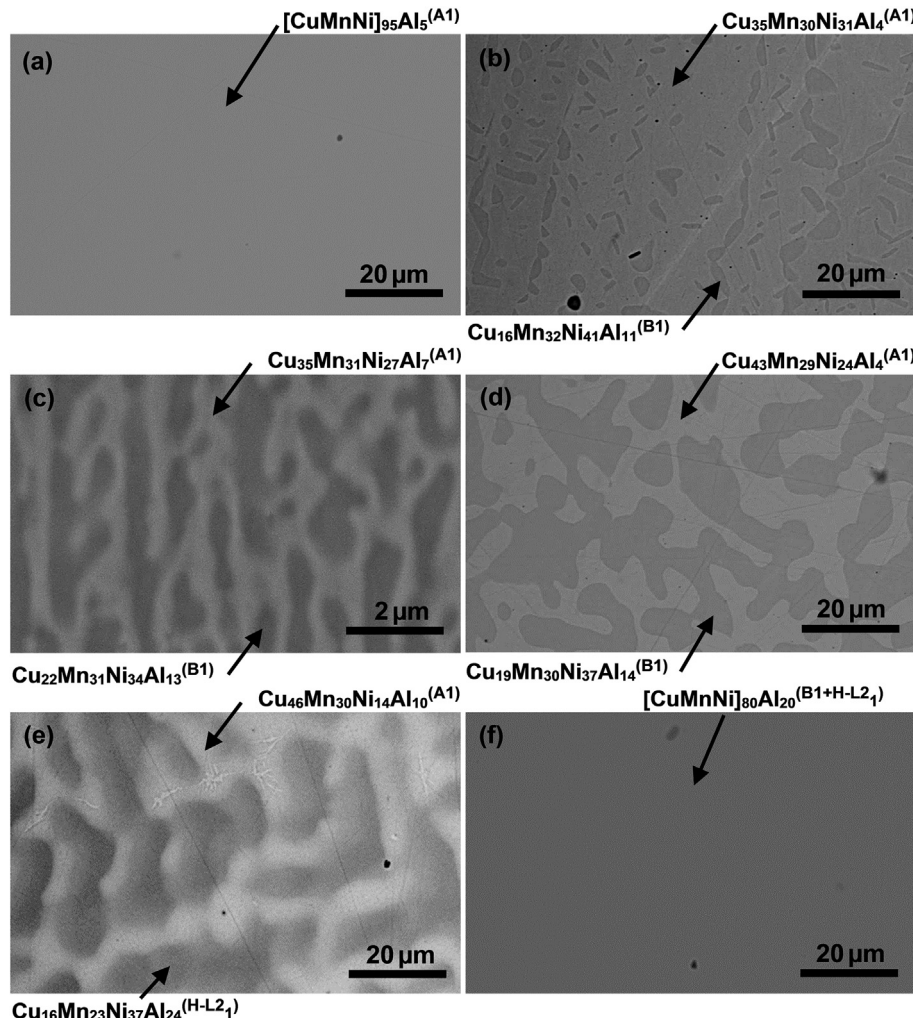


Fig. 2. Backscattered SEM images of: [CuMnNi]₉₅Al₅ in the (a) as-cast and (b) heat treated state, [CuMnNi]₉₀Al₁₀ in the (c) as-cast and (d) heat treated state and [CuMnNi]₈₀Al₂₀ in (e) as-cast and (f) heat treated state, each indicating the approximate composition (using EDS) and crystal structure of the phases present.

(rapid cooling). However, upon a heat treatment at 850 °C for 18 h, this alloy decomposes into two fcc-type phases, which can be clearly seen in Fig. 2(b). The lighter, higher volume fraction phase is a disordered fcc (A1) phase with an approximate composition (according to EDS results) of Cu₃₅Mn₃₀Ni₃₁Al₄. The second, darker phase with a much lower volume fraction indexes as an ordered fcc phase (B1). It is assumed to be a quaternary variant/combination of the ordered fcc L₁₂ phases Ni₃Al and Ni₃Mn, each with a high Cu solubility [22,38], with the approximate composition Cu₁₆Mn₃₂-Ni₄₁Al₁₁. The single phase microstructure seen in the as-cast state is due to the extended solubility of Al in the A1 phase at elevated temperatures. This metastable microstructure is retained during rapid cooling, however it decomposes to the “equilibrium” B1 phase upon heat treatment. This alloy also exhibits a modest increase in hardness upon heat treatment due to the presence of the harder B1 phase in its microstructure.

The [CuMnNi]₉₀Al₁₀ alloy shown in Fig. 2(c) and (d) shows a two phase microstructure in both the as-cast and heat treated conditions, with a considerably higher volume fraction of the darker B1 phase. The phase distribution in the as-cast state is quite fine, with diffuse phase boundaries and almost sub-micron phase spacing, compared to the microstructure of the heat treated sample. The increase in the sizes of phase regions and structural relaxation in the heat treated case are the probable reasons for the observed

decrease in alloy hardness. The approximate compositions of the A1 and B1 phases in the as-cast condition were found to be Cu₃₅Mn₃₁Ni₂₇Al₇ and Cu₂₂Mn₃₁Ni₃₄Al₁₃, respectively and for the heat treated state, Cu₄₃Mn₂₉Ni₂₄Al₄ and Cu₁₉Mn₃₀Ni₃₇Al₁₄, respectively. A substantial decrease of Al in the A1 phase is observed after heat treatment, and based on this result and as seen in the [CuMnNi]₉₅Al₅ alloy, the solubility limit of Al in the A1 phase is around 4 at%. Also due to the limited solubility of aluminium in the A1 phase, the volume fraction of the darker B1 phase increases slightly after heat treatment.

With an increase in Al content, the [CuMnNi]₈₀Al₂₀ alloy exhibits an as-cast structure (Fig. 2(e)) containing A1 and H-L₂₁ phases found to have compositions of approximately Cu₄₆Mn₃₀-Ni₁₄Al₁₀ and Cu₁₆Mn₂₃Ni₃₇Al₂₄, respectively. The solubility limit of Al is quite high in the A1 phase where elevated amounts of Cu and Mn are present. However, upon heat treatment alloy constituents are redistributed somewhat. At first look using EDS the alloy appears to have transformed to a single phase, however, XRD results reveal a duplex B1 + H-L₂₁ microstructure. A significant increase in alloy hardness is also observed with the introduction of the H-L₂₁ phase and this alloy is relatively brittle compared to the [CuMnNi]₉₅Al₅ and [CuMnNi]₉₀Al₁₀ alloys. Further this alloy was found to show faint magnetic attraction to the 1.1T magnet (soft magnetic properties) likely owing to the presence of the H-L₂₁ phase,

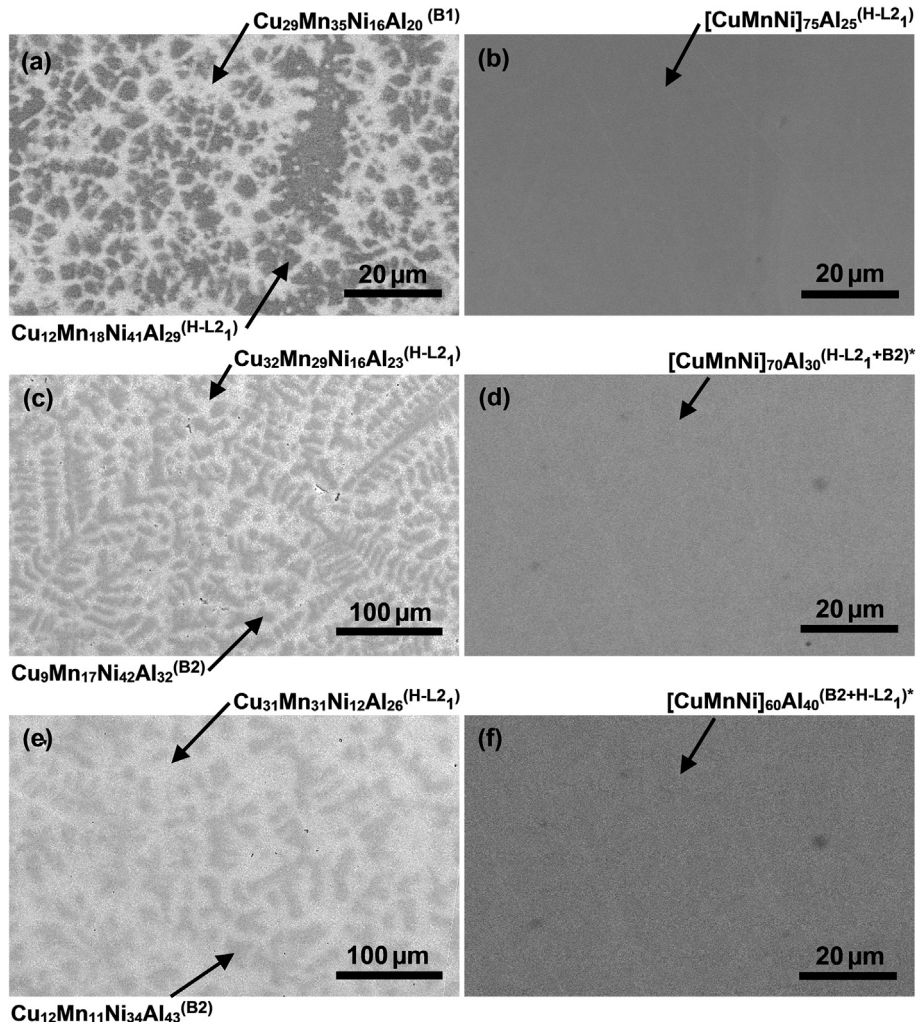


Fig. 3. Backscattered SEM images of: [CuMnNi]₇₅Al₂₅ in the (a) as-cast and (b) heat treated state, [CuMnNi]₇₀Al₃₀ in the (c) as-cast and (d) heat treated state and [CuMnNi]₆₀Al₄₀ in (e) as-cast and (f) heat treated state, each indicating the approximate composition (using EDS) and crystal structure of the phases present. *Alloys appear to exhibit a degree of spinodal decomposition.

whereas [CuMnNi]₉₅Al₅ and [CuMnNi]₉₀Al₁₀ did not.

The phase evolution in Fig. 2 shows that increasing the Al addition to the ternary CuMnNi alloys tends to stabilise the ordered quaternary B1-type phase over the A1 phase and eventually stabilises an ordered H-L_{2₁}-type phase (with a bcc sub-cell structure). However, the amount of Al in the B1 phase is always below the stoichiometric 25 at%. Here it is assumed that Al and Mn can occupy the same “large atom” sites in the L_{2₁} structure as they would in Ni₃Al or Ni₃Mn, and Cu, Ni and remaining Mn occupy the “small atom” sites creating a [Cu + Ni + Mn]₃[Al + Mn] structured compound.

Fig. 3 shows the as-cast and heat treated microstructures of the [CuMnNi]_{60–75}Al_{25–40} alloys. The [CuMnNi]₇₅Al₂₅ alloy shows a duplex as-cast solidification microstructure of B1+H-L_{2₁}, however, after heat treatment this alloy is a single phase L_{2₁}, which is somewhat expected as its stoichiometry matches an X₂YZ Heusler-type crystal structure where X = Cu + Ni (Both Ni₂MnAl and Cu₂MnAl are reported Heusler alloys [28]).

Beyond 25 at% Al addition, the alloys shift into a new phase field. [CuMnNi]₇₀Al₃₀ and [CuMnNi]₆₀Al₄₀ exhibit an as-cast and heat treated microstructure containing both the H-L_{2₁} phase and a B2-type phase where the B2 phase stoichiometry is approximately described by [Cu + Ni]₅₀[Mn + Al]₅₀. It is also apparent that as the

Ni:Al ratio increases, so too does the compositional variance of Cu and Ni in each phase, which is likely due to the higher degree of chemical attraction of the Al–Ni couple. After prolonged heat treatment the [CuMnNi]₇₀Al₃₀ and [CuMnNi]₆₀Al₄₀ alloys appear to have undergone fine-scale spinodal decomposition, which is visible in Fig. 3(d) and (f). This phenomena also has been observed in Fe–Ni–Co–Al high entropy alloys for high Al contents [39,40].

Powder XRD traces of selected [CuMnNi]_{100–x}Al_x alloys are shown in the [Supplementary material](#). In terms of lattice parameters, those of the A1 and B1 phases correlate strongly with that of typical α -brass, with the lattice parameter increasing with increasing Al content. The strongest distinction between the A1 and B1 phases is the presence of a low 2θ angle (011) plane reflection peak and (012) and (112) peaks similar to those seen in the Ni₃Al crystal. The B2 phases found in the higher Al-concentration alloys have lattice parameters similar to that of the AlNi intermetallic. The H-L_{2₁} structures also have similar lattice parameters to those observed in Cu₂MnAl Heusler alloys. Despite having different fcc and bcc structure designations, peak positions of the H-L_{2₁} and B2 phases are very similar, which is due to fact that (specific atomic ordering aside) they each have a basic bcc sub lattice structure with similar lattice parameters. It is also noted that the reflection peaks for these high entropy alloys appear considerably broad which is a

result of a high degree of lattice mismatch/strain bought about by the high fractions of different sized atoms.

The $[CuMnNi]_{95}Al_5$ and $[CuMnNi]_{90}Al_{10}$ alloys exhibit very faint soft magnetism in the presence of a magnetic field, but no more than the ternary CuMnNi alloy. The as-cast $[CuMnNi]_{80}Al_{20}$ alloy on the other hand, which contains the Heusler-type H-L₂₁ phase, exhibits considerable magnetic attraction. However, this magnetism is significantly diminished after heat treatment due to the increased volume fraction of the non-magnetic B1 phase. The $[CuMnNi]_{60-75}Al_{25-40}$ alloys all exhibit considerable magnetic attraction, as they lie directly in the H-L₂₁ or H-L₂₁+B2 phase fields of this alloy system.

Fig. 4 shows compressive stress-strain curves for the heat treated $[CuMnNi]_{95}Al_5$ and $[CuMnNi]_{90}Al_{10}$ alloys. As mentioned previously, these alloys consist of both A1 and B1 phases. The $[CuMnNi]_{95}Al_5$ alloy, with a lower volume fraction of the B1 phase yields at around 330 MPa and does not fail before 45% compressive strain (test cut short due to load cell limitations), whereas the $[CuMnNi]_{90}Al_{10}$ alloy has a yield strength of approximately 520 MPa and fails at a compressive strain of 40%. The deformed $[CuMnNi]_{90}Al_{10}$ sample microstructure in the inset of Fig. 4 clearly shows that the lighter A1 phase is considerably softer than the darker B1 phase and has been extruded from between the B1 phase regions.

4.3. Cu–Mn–Ni–Sn quaternary alloy system

Table 2 lists the range of alloys prepared in the $[CuMnNi]_{100-x}Sn_x$ quaternary alloy system, along with the microstructural phases present and hardnesses in the as-cast and heat treated conditions. Fig. 5 shows the as-cast and heat treated microstructures of the $[CuMnNi]_{100-x}Sn_x$ alloys examined.

The as-cast $[CuMnNi]_{95}Sn_5$ alloy has a predominantly A1-type microstructure (dark phase), with an approximate composition of $Cu_{34}Mn_{32}Ni_{31}Sn_3$, and a small amount of the H-L₂₁ second phase (lighter phase) with an approximate composition of $Cu_{23}Mn_{24-Ni}_{32}Sn_{21}$. The boundaries between phases are notably diffuse with a large composition gradient. In the heat treated state, the phase boundaries become more well-defined, and the second phase much more spherical. The composition of the darker A1 phase shifts to $Cu_{40}Mn_{32}Ni_{26}Sn_4$ and the lighter H-L₂₁ phase shifts to $Cu_{15}Mn_{24}Ni_{39}Sn_{22}$.

The as-cast $[CuMnNi]_{90}Sn_{10}$ alloy also consists of the A1 phase (composition approximately $Cu_{41}Mn_{29}Ni_{26}Sn_4$) and H-L₂₁ phase

(approximately $Cu_{17}Mn_{31}Ni_{36}Sn_{16}$). Upon heat treating, the A1 phase composition shifts marginally to $Cu_{40}Mn_{30}Ni_{26}Sn_4$, and the H-L₂₁ phase shifts to a more Ni- and Sn-rich composition of $Cu_{16}Mn_{25}Ni_{38}Sn_{21}$.

The as-cast $[CuMnNi]_{80}Sn_{20}$ microstructure consists predominantly of the lighter ordered H-L₂₁-type phase with a composition of $Cu_{14}Mn_{28}Ni_{34}Sn_{24}$ and the darker A1 phase residing between the large dendrites with a composition of $Cu_{57}Mn_{25}Ni_{10}Sn_8$. After heat treatment the H-L₂₁ phase morphology becomes more spherical and the composition shifts to approximately $Cu_{16}Mn_{24}Ni_{35}Sn_{25}$ with a small amount of the darker A1 phase between the spherical boundaries, now with a composition of approximately $Cu_{35}Mn_{30}Ni_{31}Sn_{4}$.

The equiatomic $[CuMnNi]_{75}Sn_{25}$ alloy appears to cast as a single H-L₂₁ phase with only minor composition deviations of 2 at% within the microstructure. Upon heat treatment, this alloy remains predominantly single phase (slightly enriched in Ni) with a very small volume fraction (<1 vol.%) of the B2 phase segregating to grain boundaries with an approximate composition of $Cu_{24}Mn_{7-Ni}_{23}Sn_{46}$. A single phase H-L₂₁ type of microstructure is somewhat expected for this alloy composition given the X₂YZ stoichiometry of the Heusler phase, where X = Cu + Ni, Y = Mn and Z = Sn.

The solubility limit of Sn in the A1 phase after heat treatment is approximately 4 at%, which is similar to the solubility of Al in the $[CuMnNi]_{100-x}Al_x$ quaternary alloys. The orthorhombic- or hexagonal-type phases present in the binary systems appear to have been “lost” and the H-L₂₁-type phase stabilises in these high entropy alloys. There is no evidence of an ordered B1 phase that is predicted in the equilibrium ternary CuMnNi alloy and found in the Al-lean $[CuMnNi]_{100-x}Al_x$ alloys. Rather, the transition to the H-L₂₁ (again with its bcc sub unit cell) is immediate, which may be a result of crystal lattice strain/topological instability, as the Sn atom is considerably larger than Al.

Powder XRD traces (see [Supplementary material](#)) for the $[CuMnNi]_{90}Sn_{10}$ and $[CuMnNi]_{75}Sn_{25}$ alloys represent the A1 + H-L₂₁ and H-L₂₁ phase fields observed within this system. Interestingly, the $[CuMnNi]_{75}Sn_{25}$ alloy, which is > 99 vol.% H-L₂₁ shows additional peak reflections when compared to the trace for $[CuMnNi]_{75}Al_{25}$ and is more closely akin to the Co_2MnTi crystal structure, which may be an indicator of additional site-specific structural ordering of Cu and Ni within the Heusler lattice.

Generally, alloy hardness increases with increasing Sn content, i.e. with increase in volume fraction of the H-L₂₁ phase within the microstructure. For the $[CuMnNi]_{90-95}Sn_{5-10}$ alloys, where the volume fraction of the A1 phase is higher than that of the H-L₂₁ phase, hardness was found to decrease upon heat treatment due to the redistribution of Sn in the microstructure resulting in a significant reduction in the volume fraction of the H-L₂₁ phase. However a reverse trend is observed upon heat treatment for alloys where the H-L₂₁ phase is dominant within the microstructure. This is likely a result of the annihilation of lattice defects and extended lattice ordering, which would result in an increase in hardness at the expense of ductility within this already quite brittle phase.

Fig. 6 shows the compressive stress-strain curves of the $[CuMnNi]_{95}Sn_5$ and $[CuMnNi]_{90}Sn_{10}$ alloys. There is a clear increase in the strength and stiffness of the alloys with the increase in the volume fraction of the H-L₂₁ phase, however, the compressive ductility of the $[CuMnNi]_{90}Sn_{10}$ alloy is around 20%, whereas $[CuMnNi]_{95}Sn_5$ exhibits >63% compressive ductility (test concluded prior to sample failure due to load cell limit). The inset in Fig. 6 is a backscattered SEM image of the deformed sample, highlighting the brittle nature of the H-L₂₁ phase by the high degree of cracking.

All $[CuMnNi]_{100-x}Sn_x$ quaternary alloys prepared in this work exhibited magnetic attraction (soft magnetism) that increases with volume fraction of the H-L₂₁ phase.

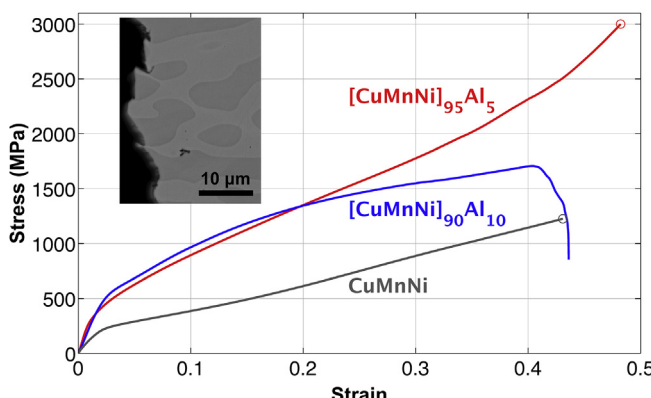


Fig. 4. Compression stress–strain curves of CuMnNi and selected $[CuMnNi]_{100-x}Al_x$ alloys in their heat-treated condition. Circles at the ends of curves indicate tests stopped before failure. Inset: backscattered SEM image of the deformed $[CuMnNi]_{90}Al_{10}$ sample microstructure showing softer A1 phase extruded between B1 phase regions.

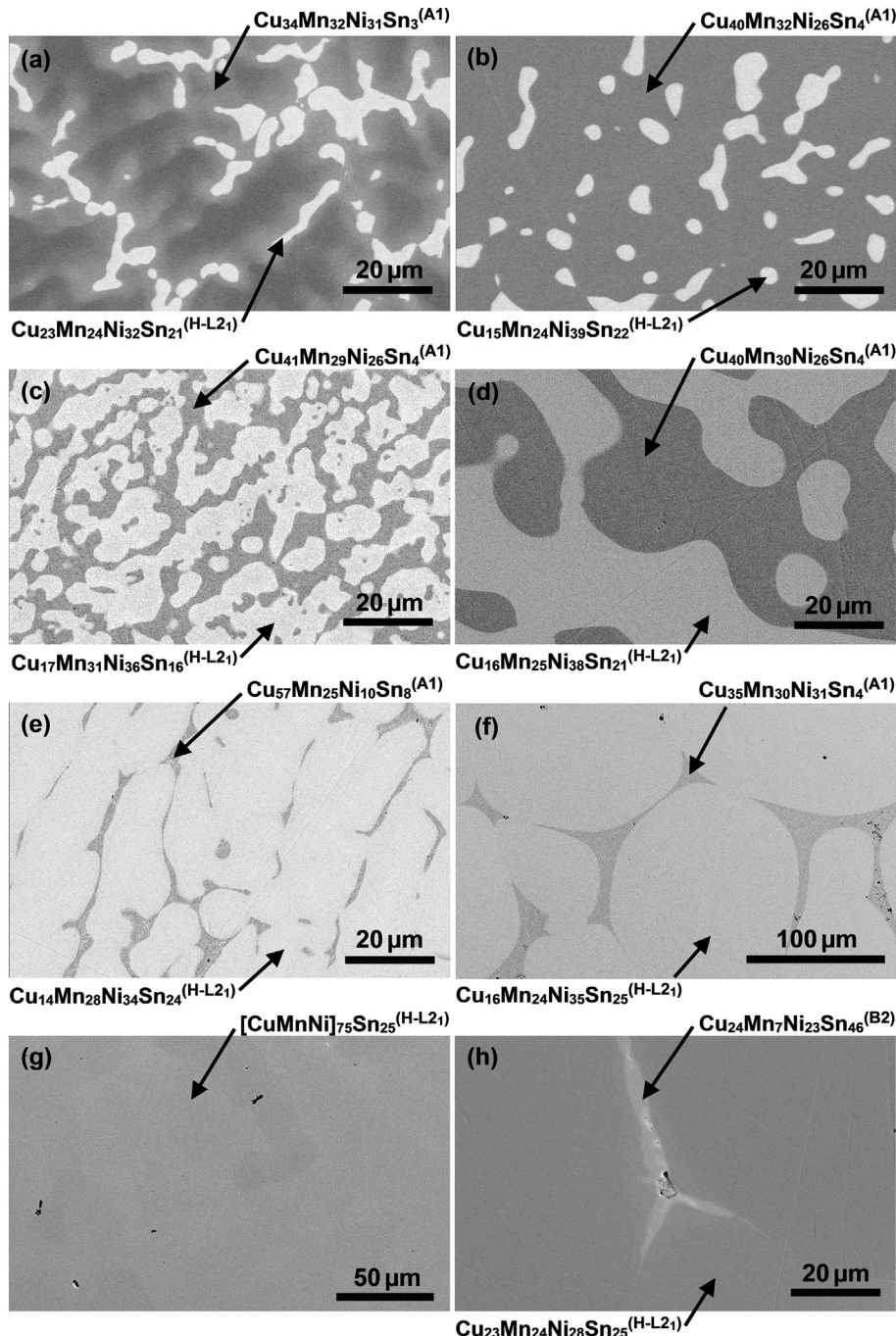


Fig. 5. Backscattered SEM images of: [CuMnNi]₉₅Sn₅ in the (a) as-cast and (b) heat treated state, [CuMnNi]₉₀Sn₁₀ in the (c) as-cast and (d) heat treated state, [CuMnNi]₈₀Sn₂₀ in (e) as-cast and (f) heat treated state and [CuMnNi]₇₅Sn₂₅ (g) as-cast and (h) heat treated state, each indicating the approximate composition (using EDS) and crystal structures of the phases present.

4.4. Cu–Mn–Ni–Zn quaternary alloys

Table 3 lists the range of alloys prepared in the [CuMnNi]_{100-x}Zn_x quaternary alloy system, along with the microstructural phases present and hardnesses in the as-cast and heat treated conditions. Lower Zn content alloys were not attempted due to the high processing temperatures required and high Zn losses due to evaporation. Fig. 7 shows acid-etched as-cast and heat treated microstructures of selected [CuMnNi]_{100-x}Zn_x alloys examined. This quaternary alloy system most closely follows the phase trends of traditional Cu–Zn brasses.

The [CuMnNi]₈₀Zn₂₀ and equiatomic [CuMnNi]₇₅Zn₂₅ alloys each display a dendritic solidification microstructure (single phase A1) within larger grains (see Fig. 7(a)), much like a typical Cu–Zn brass (keeping in mind that these alloys were produced in an induction furnace and experienced a much slower cooling rate than the non-Zn containing alloys). Upon heat treatment, the dendritic microstructure is dissolved and a large-grained, uniform A1 microstructure is observed for each case, an example of which is shown in Fig. 7(b).

With an increase in Zn content, the presence of the B2 (β) phase is observed. The heat treated [CuMnNi]₆₅Zn₃₅ and [CuMnNi]₆₀Zn₄₀

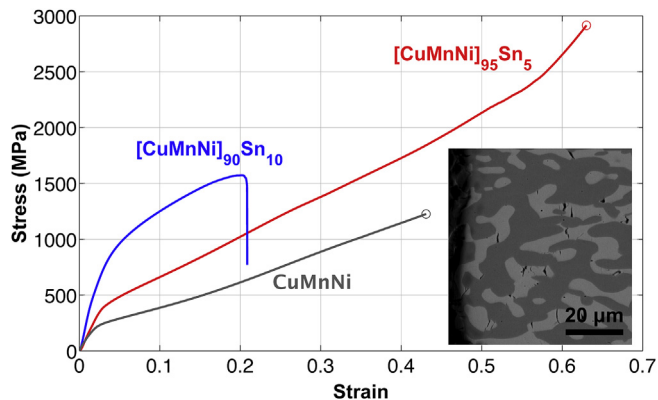


Fig. 6. Compressive stress–strain curves of the heat treated CuMnNi, $[CuMnNi]_{95}Sn_5$ and $[CuMnNi]_{90}Sn_{10}$ alloys. Circles at the ends of curves indicate tests stopped before failure. Inset: backscattered SEM image of the deformed $[CuMnNi]_{90}Sn_{10}$ alloy microstructure showing substantial cracking in the H-L2₁ phase.

alloys shown in Fig. 7(c) and (d), which reside within the A1 + B2 (α + β) phase field, naturally show an increasing amount of the B2 phase with increasing Zn content.

Powder XRD traces for the $[CuMnNi]_{100-x}Zn_x$ alloys, with indexed peaks attributed to the crystallographic planes of the A1 and B2 phases (α + β) present in this alloy series, are in Supplementary material. The A1 phase related peaks are present in all alloys, and the fcc structures were confirmed using EBSD. With increasing Zn content, the A1 indexed peaks shift to slightly lower 2θ angles and tend to become broader, which would be expected in a random fcc lattice with an increase in the concentration of a larger atom due to a larger average lattice parameter and greater lattice misfit. The B2 phase peaks are only faintly evident in the $[CuMnNi]_{65}Zn_{35}$ alloy, yet appear quite intensely in the

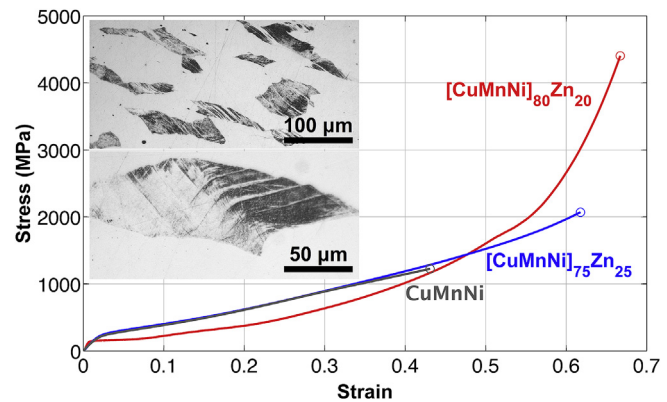


Fig. 8. Compressive stress strain curves for CuMnNi and selected heat treated $[CuMnNi]_{100-x}Zn_x$ alloys examined in this study. Circles at the ends of curves indicate tests stopped before failure. Insets: optical micrographs of the compressed $[CuMnNi]_{75}Zn_{25}$ sample indicating the presence of deformation twins.

$[CuMnNi]_{60}Zn_{40}$ alloy due to the relative volume fraction of this phase present in each sample.

Generally, the hardness of these alloys increases with increasing Zn content. For the case of the purely A1 alloys $[CuMnNi]_{80}Zn_{20}$ and $[CuMnNi]_{75}Zn_{25}$, this is due to an increase in solution strengthening, brought about by the internal strains induced within the lattice due to the lattice misfit associated with the larger Zn atom. An additional jump in the hardness is observed with the presence and increasing volume fraction of the harder B2 phase in the $[CuMnNi]_{65}Zn_{35}$ and $[CuMnNi]_{60}Zn_{40}$ alloys. The hardnesses of these alloys are somewhat higher than the equivalent Cu–Zn brasses (C26000), which typically display a hardness of 100HV for an α -brass with a Zn content of 28–32 at% [41] and 146HV for a typical (α + β)-brass (C46400) with a Zn content of 38–40 at% [41].

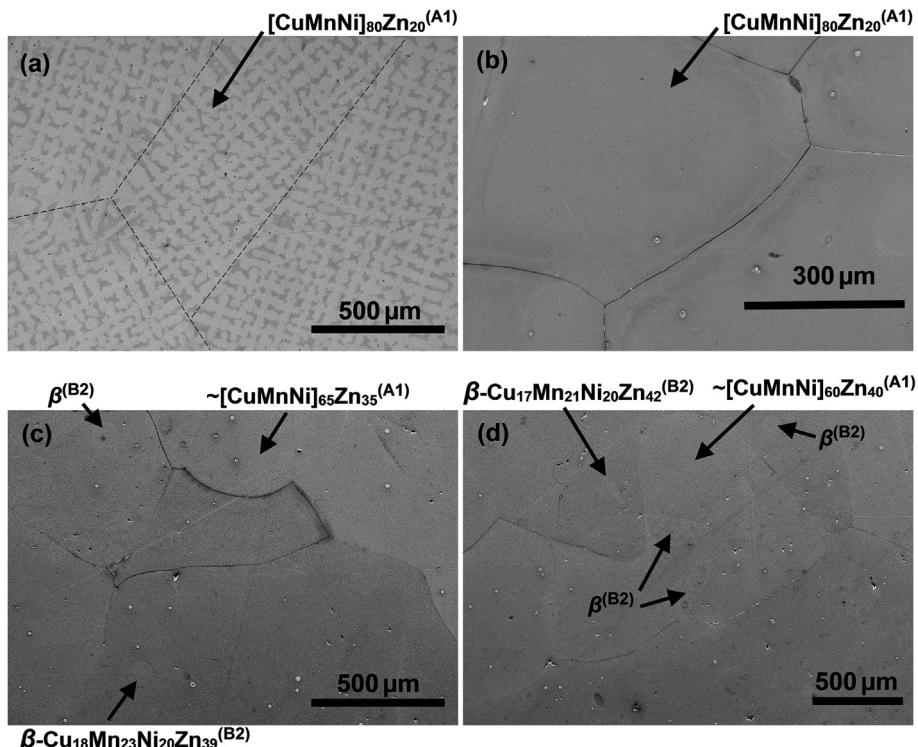


Fig. 7. (a) An optical micrograph of acid-etched, as-cast $[CuMnNi]_{80}Zn_{20}$ alloy showing a sub-grain dendritic solidification microstructure within much larger grains (all single phase A1), (b) a secondary electron image of acid etched, heat treated $[CuMnNi]_{80}Zn_{20}$ showing large uniform A1 grains, (c) a secondary electron image of acid-etched and heat treated $[CuMnNi]_{65}Zn_{35}$ and (d) $[CuMnNi]_{60}Zn_{40}$ alloys indicating small islands of the B2 phase.

in the annealed condition.

Fig. 8 shows the compressive stress strain curves of the $[CuMnNi]_{80}Zn_{20}$ and $[CuMnNi]_{75}Zn_{25}$ alloys. The yield strengths of these single phase Zn-containing quaternary alloys are considerably lower than those observed in the multi-phase Al- and Sn-containing alloys, and for the lower Zn concentration appreciably lower than the base ternary system. This could be due to the presence of a more energetically favoured twinning mechanism evident in the insets of **Fig. 8** or a change in stacking fault energy with the addition of Zn.

None of the $[CuMnNi]_{100-x}Zn_x$ quaternary alloys produced in

this work showed signs of the magnetism observed in the $[CuMnNi]_{100-x}Al_x$ and $[CuMnNi]_{100-x}Sn_x$ quaternary alloys.

4.5. Cu–Mn–Ni–[Al,Sn,Zn] quinary alloys

Table 4 lists the range of alloys prepared in the $[CuMnNi]_{100-x-y-z}Al_xSn_yZn_z$ quinary alloy systems, along with the microstructural phases present and hardnesses in the as-cast and heat treated conditions. **Figs. 9 and 10** show the as-cast and heat treated microstructures of the quinary alloys in **Table 4**. As-cast and heat treated hardness values are related to those observed in the

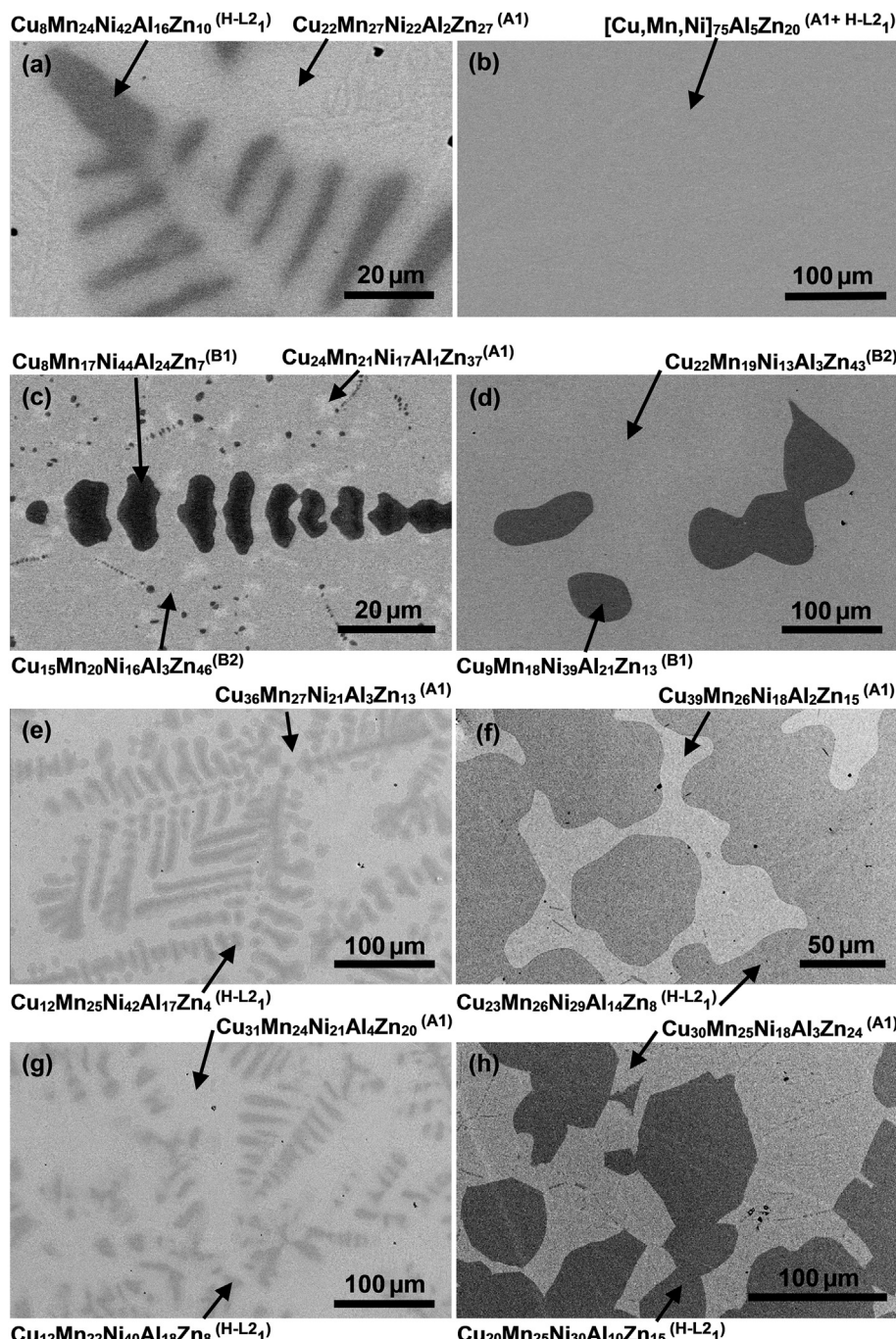


Fig. 9. Backscattered SEM images of: $[CuMnNi]_{75}Al_5Zn_{20}$ in the (a) as-cast and (b) heat treated state; $[CuMnNi]_{60}Al_5Zn_{35}$ in the (c) as-cast and (d) heat treated state, $[CuMnNi]_{80}Al_{10}Zn_{10}$ in the (e) as-cast and (f) heat treated state and $[CuMnNi]_{70}Al_{10}Zn_{20}$ in the (g) as-cast and (h) heat treated state. Approximate compositions (using EDS) and crystal structures of the phases present are indicated.

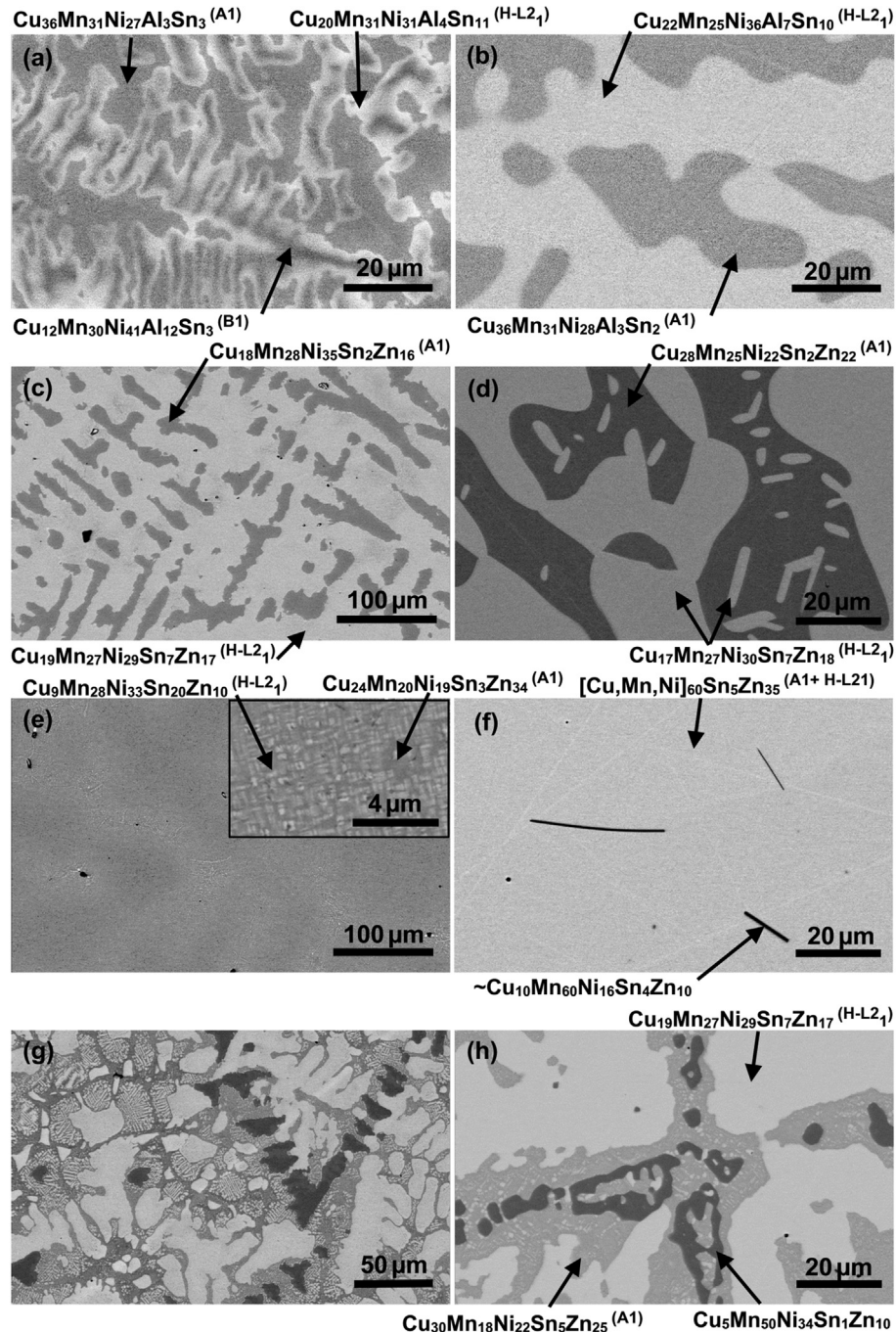


Fig. 10. Backscattered SEM images of: $[CuMnNi]_{90}Al_5Sn_5$ in the (a) as-cast and (b) heat treated state; $[CuMnNi]_{75}Sn_5Zn_{20}$ in the (c) as-cast and (d) heat treated state, $[CuMnNi]_{60}Sn_5Zn_{35}$ in the (e) as-cast and (f) heat treated state and $[CuMnNi]_{70}Sn_{10}Zn_{20}$ in the (g) as-cast and (h) heat treated state. Approximate compositions (using EDS) and crystal structures of the phases present are indicated.

quaternary alloy systems, often lying at values intermediate to the two quaternary counterparts and highly dependent on the volume fraction of the H-L2₁ phase.

Fig. 9 shows the microstructures of the as-cast and heat treated $[CuMnNi]_{100-x-z}Al_xZn_z$ quinary alloys. Despite the high fraction of Zn in $[CuMnNi]_{75}Al_5Zn_{20}$ (Fig. 9(a) and (b)), this alloy still segregates into a high entropy version of the H-L2₁-type phase rich in Al and Ni, low in Zn, plus an A1 phase high in Zn and Cu, low in Al. These two phases are indistinguishable through backscattered electron contrast, however two distinct phases are detected by XRD. Interestingly quinary $[CuMnNi]_{100-x-y}Al_xZn_y$ alloys with 5 at%

Al do not show the higher degree of order peaks in XRD patterns belonging to the H-L2₁ phase, likely due to a lower volume fraction or higher degree of structural disorder in this case.

A further increase in Zn in the $[CuMnNi]_{60}Al_5Zn_{35}$ alloy produces a multi-phase as-cast microstructure seen in Fig. 9(c) (A1+B1+B2). However, upon heat treatment (Fig. 9(d)) it converts to a predominantly B2 microstructure where, based on phase stoichiometry, Cu, Mn and Ni occupy a particular lattice site, and Al and Zn the other. There is also a small volume fraction of B1 phase found in these heat treated samples (less than 5%), where, based on stoichiometry, Zn could occupy the Cu, Mn or Ni lattice sites in this

phase type.

An increase in Al content in the $[CuMnNi]_{100-x-z}Al_xZn_z$ quinary alloys stabilises the H-L₂₁ phase, and a significant volume fraction of this phase can be seen for the $[CuMnNi]_{70-80}Al_{10}Zn_{10-20}$ alloys in Fig. 9(e)–(h). Despite these alloys containing a considerable volume fraction of the H-L₂₁ phase, they are only faintly magnetic, indicating that the substitution of Zn for Al in the Heusler structure leads to a collapse of the magnetic moments.

Fig. 10(a) and (b) shows the microstructures of the as-cast and heat treated $[CuMnNi]_{90}Al_5Sn_5$ alloy. Initially a three-phase as-cast microstructure ($A1 + B1 + H-L2_1$), after heat treatment this alloy converts to a two phase $A1 + H-L2_1$ alloy, where Al and Sn occupy the Z sites in the X_2YZ Heusler structure, despite the Al and Sn contents being lower than expected. This alloy also maintains the magnetic properties inherent to Heusler ordering.

The $[CuMnNi]_{100-x-y}Sn_xZn_y$ quinary alloys exhibit a predominantly $A1 + H-L2_1$ microstructure, which is well defined for the as-cast and heat treated $[CuMnNi]_{75}Sn_5Zn_{20}$ alloy. However with an increase in Zn content as in the $[CuMnNi]_{60}Sn_5Zn_{35}$ alloy, the morphology of these phases changes to a basket-weave type arrangement, which can be seen in the inset of Fig. 10(e). Upon heat treatment of this alloy, a third, needle-like phase rich in Mn precipitates, seen in Fig. 10(f). When the Sn content is increased as in the $[CuMnNi]_{70}Sn_{10}Zn_{20}$ alloy, for the first time in this work a multi-phase as-cast eutectic microstructure is observed, likely related to the low-melting point eutectic reaction between Sn and Zn. Upon heat treatment, the eutectic type morphology is dissolved and a three-phase microstructure containing $A1 + H-L2_1$ forms, and again a Mn-rich phase evolves.

Like the $[CuMnNi]_{100-x-z}Al_xZn_z$ quinary alloys, based on stoichiometry it would seem that Zn can be successfully substituted for Sn in the Heusler structure. However, in this case all three $[CuMnNi]_{100-x-y}Sn_xZn_y$ quinary alloys exhibit strong magnetic attraction, comparable to that observed for the $[CuMnNi]_{100-x}Sn_x$ quaternary alloys, which indicates that this particular substitution does not dramatically affect the magnetic coupling within the Heusler structure. Of all the alloys tested, only in $[CuMnNi]_{100-y-z}Sn_yZn_z$ alloys is there a slight residual magnetisation, indicating a slightly “harder” component to their magnetisation.

The *Supplementary material* contains indexed XRD traces for selected $[CuMnNi]_{100-x-y-z}Al_xSn_yZn_z$ quinary alloys, confirming the prior mentioned phase constitutions.

4.6. General discussion

In this work it has been observed that with incremental addition of a fourth, larger element (Zn, Al or Sn) to the base CuMnNi solid solution composition, alloys tend to transit from a purely single phase fcc microstructure to a fcc + bcc microstructure (where A2 and B2 are bcc and the high entropy H-L₂₁ phase essentially has a bcc sub-unit cell) to a purely bcc phase microstructure. This is similar to the CoCrFeMnNi solid solution high entropy alloy systems, where upon the addition of a larger or considerably electronically different element (such as Al or Ti) lattice types transit from fcc to fcc + bcc and eventually to completely bcc [42]. Crystal lattice types of transition metals are closely linked to electronic structure: elements with partially filled d-shells have a tendency to form more attractive covalent/directional bonds due to d-d bond hybridisation, hence V, Cr and Fe exhibit a bcc lattice type (Mn is a complex exception [43]). As the d-shell is incrementally filled with electrons these interactions lessen, and essentially interatomic potentials become more repulsive, hence more efficient packing structures like hcp (Co) and fcc (Ni and Cu) are preferred [44].

Additions of both Al and Sn have dramatic effects on the strengths of the A1-type solid solutions and have a high tendency

to stabilise ordering in both fcc and bcc phases. Both Al and Sn have a high valence electron density, with electrons present in their outermost p and s orbitals (Al = [Ne] 3s² 3p¹, Sn = [Kr] 4d¹⁰ 5s² 5p²), which indicates a high ionisation tendency, i.e. a preference to interact strongly or transfer electrons to transition metals with non-filled d-shells. This greatly increases the degree of covalency and directionality in bonding within an alloy and eventually the formation of ordered intermetallic compounds. Further, both Al (atomic radius in pure metal ~141 pm) and Sn (radius ~155 pm) are considerably larger than the 3d transition metals used (Mn radius ~128 pm, Ni ~126 pm, Cu ~128 pm), which has a strong effect on crystal lattice strain [45,46]. Hence, with an incremental increase in bond covalency, directionality and lattice strain with increasing Al and/or Sn content, the fcc solid solutions in these alloys are progressively strengthened. This continues to a point where the fcc structure becomes both electronically and topologically unstable. To accommodate this instability, the fcc phase transforms to a simple or ordered bcc structure that can accommodate greater topological lattice strain (the bcc structure is less efficiently packed than the fcc structure) and bond directionality.

On the other hand, Zn has a considerably lower impact on strengthening/work hardening and the fcc to bcc phase transition in these alloys (and generally follows the trend of regular Cu-Zn brasses for increased Zn content). Zn has a full d-shell and two s electrons in its outer electronic structure ([Ar] 3d¹⁰ 4s²) and is only slightly larger in terms of atomic radius (~135 pm) than Cu, Mn and Ni. Hence there is a lesser degree of bond hybridisation between Zn and the transition metals in general and less lattice strain. This is also the probable origin of the greater solubility limit of Zn in the base CuMnNi fcc microstructure and in Cu-Zn, Mn-Zn and Ni-Zn binary systems, along with the lack of the intermediate $[Cu,Mn,-Ni]_3[Al,Sn]$ type intermetallic phases.

For all of the quaternary alloys studied here, the degrees of bond interaction (or bond enthalpy) between the elements of the base ternary system and the fourth element scale such that Ni > Mn > Cu. Of the three solute additions to the base ternary alloy, bond interactions, directionality and hence bcc stabilisation scale such that Sn > Al > Zn. This follows trends in both electron density and atomic size. It is also the likely reason that Ni tends to segregate with Al and Sn in the ordered B1 and B2 phases, and Cu contents are generally higher in the disordered A1 phases. The combination of electron density and lattice strain is also the likely reason that the transformation from fcc to fcc + bcc requires the lowest atomic percent addition of Sn, followed by Al and finally Zn.

Of the quaternary alloys, it is those that do have the highest entropy that indeed form a single phase microstructure. A single phase microstructure was achieved for the equiatomic $[CuMnNi]_{75}Al_{25}$ and $[CuMnNi]_{75}Sn_{25}$ alloys. The $[CuMnNi]_{70-80}Zn_{20-25}$ alloys also exhibited a single phase A1-type microstructure with no evidence of the ordered B1 phase found in Al-lean quaternaries. However, considering the phase equilibria surrounding these alloys in relation to their binary phase diagrams and the mutual solubility of the Cu-Mn-Ni base, these results may have been expected. In all cases, the quinary alloys, often with higher entropy than the quaternary alloys, do not form single phases. Although an increase in chemical entropy may play a role in the stabilisation of single phase microstructures, the formation of such a phase in the cases of these alloys is more a result of the mutual (binary and ternary) solid solubility of the elements present, combined with preferred topological or electronic ordering aspects of the preferred base crystal lattice.

5. Conclusions

A range of new, high entropy brasses and bronzes containing one or two simple multicomponent phases has been produced. It is

clear that despite the high entropy of the alloy systems presented, simple, disordered fcc or bcc phases are not necessarily the result of high entropy, and instead the specific electronic nature of constituents and topology play significant roles in phase evolution and structural ordering. Although single or duplex phase microstructures can be formed in these multicomponent systems, these are considered extensions of the mutual solubility of specific alloy additions to the base CuMnNi alloy at particular concentrations, rather than a direct result of entropy. In most cases phase evolution tends to follow the sequences common to the respective binary Cu-X, Mn-X and Ni-X systems, essentially giving rise to multicomponent, often ordered, fcc- or bcc-based phases.

These novel alloys exhibit considerable strength, hardness and ductility improvements over standard commercial brasses and in some cases unique soft magnetic properties. The precise crystal structures determined using high resolution TEM and first principles modelling, and the unique magnetic properties of these high entropy brasses and bronzes shall be reported elsewhere shortly.

Acknowledgements

The authors gratefully acknowledge the ongoing financial contributions and academic support of Professor Michael Ferry (UNSW) to this project and the staff of the Mark Wainwright Analytical Centre and Professor Paul Munroe for their ongoing assistance. Thank you to the US National Science Foundation (Grant: OISE-1261525), the Laspa Fellowship at Harvey Mudd College and the Australian Research Council (Grant: DE120102588) for the funding of this research.

Appendix A. Supplementary data

Supplementary data related to this article can be found at <http://dx.doi.org/10.1016/j.jallcom.2015.07.285>.

References

- [1] C.P. Thornton, Of brass and bronze in prehistoric southwest Asia, in: S. La Niece, D. Hook, P.T. Craddock (Eds.), *Metals and Mines: Studies in Archaeometallurgy*, Archetype Publications, London, 2007, pp. 123–135.
- [2] W. Zhou, The emergence and development of brass smelting techniques in China, *Bull. Met. Mus. Jpn. Inst. Met.* 34 (2001) 87–98.
- [3] P.T. Craddock, K. Eckstein, Production of brass in antiquity by direct reduction, in: P.T. Craddock, J. Lang (Eds.), *Mining and Metal Production through the Ages*, British Museum, London, 2003, pp. 226–227.
- [4] T. Rehren, M. Martinón-Torres, *Naturam ars imitata: European brassmaking between craft and science*, in: M. Martinón-Torres, T. Rehren (Eds.), *Archaeology, History and Science: Integrating Approaches to Ancient Materials*, Left Coast Press, Walnut Creek, 2008, pp. 167–188.
- [5] J.R. Davis (Ed.), *ASM Handbook: Copper and Copper Alloys*, ASM International, 2001, pp. 3–9.
- [6] W.F. Smith, *Structure and Properties of Engineering Alloys*, second ed., McGraw-Hill, 1993.
- [7] B. Cantor, I.T.H. Chang, P. Knight, A.J.B. Vincent, Microstructural development in equiatomic multicomponent alloys, *Mater. Sci. Eng. A* 375–377 (2004) 213–218.
- [8] F. Otto, Y. Yang, H. Bei, E.P. George, Relative effects of enthalpy and entropy on the phase stability of equiatomic high-entropy alloys, *Acta Mater.* 61 (2013) 2628–2638.
- [9] C. Zhu, Z.P. Lu, T.G. Nieh, Incipient plasticity and dislocation nucleation of FeCoCrNiMn high-entropy alloy, *Acta Mater.* 61 (2013) 2993–3001.
- [10] G.A. Salishchev, M.A. Tikhonovsky, D.G. Shaysultanov, N.D. Stepanov, A.V. Kuznetsov, I.V. Kolodiy, A.S. Tortika, O.N. Senkov, Effect of Mn and V on structure and mechanical properties of high-entropy alloys based on CoCrFeNi system, *J. Alloys Compd.* 591 (2014) 11–21.
- [11] Y.J. Zhou, Y. Zhang, Y.L. Wang, G.L. Chen, Solid solution alloys of AlCoCrFeNiTi_x with excellent room-temperature mechanical properties, *Appl. Phys. Lett.* 90 (2007) 181904.
- [12] Y. Zhang, X. Yang, P.K. Liaw, Alloy design and properties optimization of high-entropy alloys, *J. Mater.* 64 (2012) 830–838.
- [13] M.A. Hemphill, T. Yuan, G.Y. Wang, J.W. Yeh, C.W. Tsai, A. Chuang, P.K. Liaw, Fatigue behavior of Al_{0.5}CoCrCuFeNi high entropy alloys, *Acta Mater.* 60 (2012) 5723–5734.
- [14] B.A. Welk, R.E.A. Williams, G.B. Viswanathan, M.A. Gibson, P.K. Liaw, H.L. Fraser, Nature of the interfaces between the constituent phases in the high entropy alloy CoCrCuFeNiAl, *Ultramicroscopy* 134 (2013) 193–199.
- [15] W. Guo, W. Dmowski, J.-Y. Noh, P. Rack, P. Liaw, T. Egami, Local atomic structure of a high-entropy alloy: an x-ray and neutron scattering study, *Metall. Mater. Trans. A* 44 (2013) 1994–1997.
- [16] O.N. Senkov, G.B. Wilks, D.B. Miracle, C.P. Chuang, P.K. Liaw, Refractory high-entropy alloys, *Intermetallics* 18 (2010) 1758–1765.
- [17] O.N. Senkov, J.M. Scott, S.V. Senkova, D.B. Miracle, C.F. Woodward, Microstructure and room temperature properties of a high-entropy TaNbHfZrTi alloy, *J. Alloys Compd.* 509 (2011) 6043–6048.
- [18] O.N. Senkov, S.V. Senkova, C. Woodward, D.B. Miracle, Low-density, refractory multi-principal element alloys of the Cr–Nb–Ti–V–Zr system: Microstructure and phase analysis, *Acta Mater.* 61 (2013) 1545–1557.
- [19] O.N. Senkov, S.V. Senkova, C. Woodward, Effect of aluminum on the microstructure and properties of two refractory high-entropy alloys, *Acta Mater.* 68 (2014) 214–228.
- [20] A. Takeuchi, K. Amiya, T. Wada, K. Yubuta, W. Zhang, High-entropy alloys with a hexagonal close-packed structure designed by equi-atomic alloy strategy and binary phase diagrams, *J. Mater.* 66 (2014) 1984–1992.
- [21] M. Feuerbacher, M. Heidemann, C. Thomas, Hexagonal high-entropy alloys, *Mat. Res. Lett.* 3 (2014) 1–6.
- [22] W.H. Sun, H.H. Xu, Y. Du, S.H. Liu, H.L. Chen, L.J. Zhang, B.Y. Huang, Experimental investigation and thermodynamic modeling of the Cu–Mn–Ni system, *Calphad* 33 (2009) 642–649.
- [23] K.P. Gupta, Phase Diagrams Ternary Nickel Alloys, *Indian Inst. Metals, Calcutta*, 1990.
- [24] H. Okamoto, Cu–Mn (Copper–Manganese), in: second ed., in: T.B. Massalski (Ed.), *Binary Alloy Phase Diagrams*, vol. 2, ASM Alloy Phase Diagrams Center, 1990, pp. 1435–1436.
- [25] N.A. Gokcen, Mn–Ni (Manganese–Nickel), in: second ed., in: T.B. Massalski (Ed.), *Binary Alloy Phase Diagrams*, vol. 2, ASM Alloy Phase Diagrams Center, 1990, pp. 2580–2583.
- [26] J.L. Murray, Al–Cu (Aluminum–Copper), in: second ed., in: T.B. Massalski (Ed.), *Binary Alloy Phase Diagrams*, vol. 2, ASM Alloy Phase Diagrams Center, 1990, pp. 141–143.
- [27] I. Ansara, N. Dupin, H.L. Lukas, B. Sundman, Thermodynamic assessment of the Al–Ni system, *J. Alloys Compd.* 247 (1997) 20–30.
- [28] T. Block, M.J. Carey, B.A. Gurney, O. Jepsen, Band-structure calculations of the half-metallic ferromagnetism and structural stability of full- and half-Heusler phases, *Phys. Rev.* 70 (2004) 205114.
- [29] J.H. Shim, C.S. Oh, B.J. Lee, D.N. Lee, Thermodynamic assessment of the Cu–Sn system, *Z. Met.* 87 (1996) 205–212.
- [30] H. Okamoto, Mn–Sn (Manganese–Tin), *J. Phase Equilib.* 20 (1999) 542.
- [31] C. Schmetterer, H. Flandorfer, L.W. Richter, U. Saeed, M. Kauffmann, P. Roussel, H. Ipser, A new investigation of the system Ni–Sn, *Intermetallics* 15 (2007) 869–884.
- [32] B. Hamri, B. Abbar, A. Hamri, O. Baraka, A. Hallouche, A. Zaoui, Electronic structure and mechanical properties of X₂MnSn (X = Cu, Ni, Pd) under hydrostatic pressure: GGA+U calculations, *Comput. Condens. Matter* (2015), <http://dx.doi.org/10.1016/j.cocom.2014.12.003>.
- [33] M. Diviš, The electronic structure of Ni₃Sn and Ni₂CuSn intermetallics, *Phys. Stat. Sol. B* 173 (1992) K13–K17.
- [34] N. David, J.M. Fiorani, M. Vilas, J. Hertz, Thermodynamic reevaluation of the Cu–Zn system by electromotive force measurements in the zinc-rich part, *J. Phase Equilib.* 24 (2003) 240–248.
- [35] H. Okamoto, L.E. Tanner, Mn–Zn (Manganese–Zinc), *Bull. Alloy Phase Diag.* 11 (1990) 377–384.
- [36] H. Okamoto, Ni–Zn (Nickel–Zinc), *J. Phase Equilib.* 24 (2003) 280–281.
- [37] R. Hirschl, J. Hafner, Y. Jeanvoine, The phase diagram and electronic structure of Pd–V alloys: ab initio density functional calculations, *J. Phys. Condens. Matter* 13 (2001) 3545–3572.
- [38] A. Prince, Aluminium–copper–nickel, in: P. Villars (Ed.), *Ternary Alloys* vol. 4 (1991) 597–629. VCH.
- [39] R. Sriharitha, B.S. Murty, R.S. Kottada, Phase formation in mechanically alloyed Al_xCoCrCuFeNi (x = 0.45, 1, 2.5, 5 mol) high entropy alloys, *Intermetallics* 32 (2013) 119–126.
- [40] C.J. Tong, M.R. Chen, J.W. Yeh, S.J. Lin, S.K. Chen, T.T. Shun, S.Y. Chang, Mechanical performance of the Al_xCoCrCuFeNi high-entropy alloy system with multiprincipal elements, *Metall. Mater. Trans. A* 36 (2005) 1263–1271.
- [41] MatWeb, LLC, 2014. <http://matweb.com>.
- [42] Z. Tang, M.C. Gao, H. Diao, T. Yang, J. Liu, T. Zuo, Y. Zhang, Z. Lu, Y. Cheng, Y. Zhang, P.K. Liaw, T. Egami, Aluminum alloying effects on lattice types, microstructures, and mechanical behavior of high-entropy alloys systems, *J. Mater.* 65 (2013) 1848–1858.
- [43] D. Hobbs, J. Hafner, D. Spišák, Understanding the complex metallic element Mn. I. Crystalline and noncollinear magnetic structure of α -Mn, *Phys. Rev. B* 68 (2003) 014407.
- [44] W. Hume-Rothery, R.E. Smallman, C.W. Haworth, *The Structure of Metals and Alloys*, Metals & Metallurgy Trust, London, 1969.
- [45] T. Egami, Y. Waseda, Atomic size effect on the formability of metallic glasses, *J. Non-Cryst. Solids* 64 (1984) 113–134.
- [46] O.N. Senkov, D.B. Miracle, A topological model for metallic glass formation, *J. Non-Cryst. Solids* 317 (2003) 34–39.